photonics

MDPI

Article

Wind Profiling from Boundary Layer to Stratosphere Using a Scanning Rayleigh Doppler Lidar and a Coherent Lidar

Hengjia Liu [1], Jie Liu [2], Sijiang Wu [2], Shuhua Zhang [1], Jiawei Li [1], Chong Chen [3], Dongsong Sun [1,3] and Yuli Han [1,3,*]

[1] School of Earth and Space Sciences, University of Science and Technology of China, Hefei 230026, China; ln131632@mail.ustc.edu.cn (H.L.); jacklion@mail.ustc.edu.cn (S.Z.); curryhan@mail.ustc.edu.cn (J.L.); sds@ustc.edu.cn (D.S.)
[2] Northwest Institute of Nuclear, Xi'an 710024, China; liujie@nint.ac.cn (J.L.); wusijiang@nint.ac.cn (S.W.)
[3] Hefei National Laboratory, Hefei 230094, China; cchan@ustc.edu.cn
* Correspondence: hanyuli@ustc.edu.cn

Abstract

Accurate measurements of wind fields in the troposphere and stratosphere are essential for advancing atmospheric dynamics research, improving weather prediction, and supporting aerospace operations. However, a single Doppler lidar technique usually has limited capability to provide vertically extended wind profiles across both aerosol-rich lower altitudes and molecular-dominated higher altitudes. In this paper, we present a hybrid Doppler lidar system that combines a 355 nm scanning incoherent Rayleigh Doppler lidar with a 1550 nm coherent aerosol Doppler lidar for multi-scale wind field detection. The coherent Doppler lidar is used for boundary-layer wind retrievals, while the Rayleigh Doppler lidar, based on the double-edge technique, extends wind profiling from the upper boundary layer to approximately 40 km. Field deployments demonstrate continuous wind profiling from 50 m to 40 km, extending from the boundary layer to the stratosphere. Comparisons with radiosonde measurements show good agreement during the field campaigns, supporting the feasibility of this hybrid configuration for vertically extended wind profiling. The resulting high-resolution wind measurements across multiple atmospheric regions provide valuable data sources for studies of multi-scale circulation research, gravity wave dynamics, and climate-related atmospheric processes.

Keywords: wind profiling; scanning Rayleigh Doppler lidar; wind field; Fabry–Perot etalon interferometer

1. Introduction

The detection of wind fields in the troposphere and stratosphere plays a critical role in atmospheric dynamics research, enhancing the accuracy of numerical weather prediction and supporting aerospace operations [1,2]. Doppler lidar has become an important active remote sensing technique for atmospheric wind measurements by providing wind profiles with high spatial and temporal resolution. Among different Doppler lidar techniques, incoherent Rayleigh Doppler lidar is particularly suitable for wind measurements in molecular-dominated altitude regions, such as the upper troposphere and stratosphere [3]. Yet, aerosol interference limits the performance of incoherent Rayleigh Doppler lidars below the boundary layer. By contrast, coherent Doppler lidar, operating at longer wavelengths and exploiting aerosol backscatter, is well established for boundary layer wind measure-

Check for updates

Received: 7 April 2026
Revised: 13 May 2026
Accepted: 27 May 2026
Published: 29 May 2026

Copyright: © 2026 by the authors. Licensee MDPI, Basel, Switzerland. This article is an open access article distributed under the terms and conditions of the Creative Commons Attribution (CC BY) license.

ments. Combining these two complementary systems offers the prospect of seamless wind profiling across atmospheric regions while enhancing measurement accuracy.

Early studies established the foundation of Rayleigh Doppler wind lidar for middle-atmosphere wind measurements. In 1989, Chanin et al. demonstrated the first wind lidar system incorporating a dual-channel Fabry–Perot Interferometer (FPI), operating at a wavelength of 532 nm and capable of measuring winds between 25 and 50 km altitude [4,5]. Subsequently, Tepley reported a system utilizing a single-channel FPI as a frequency discriminator, achieving detection altitudes up to 60 km [6–9]. In 1999, Korb and his team at NASA's Goddard Space Flight Center refined the theory of the edge technique and successfully developed the Ground-based Lidar Observatory for Winds (GLOW) [10,11]. More recently, Rayleigh Doppler wind lidar techniques have been extended to both mobile ground-based and spaceborne applications. The University of Science and Technology of China (USTC) has developed mobile incoherent lidar systems for upper-tropospheric and stratospheric wind profiling [12–15], while the European Space Agency (ESA)'s Atmospheric Laser Doppler Instrument (ALADIN) mission demonstrated the capability of spaceborne direct-detection Doppler wind lidar for global wind observations [16–19]. These developments have significantly advanced wind measurements in molecular-dominated altitude regions, particularly in the upper troposphere and stratosphere.

Despite these advances, to get a comprehensive understanding of atmospheric dynamics requires bridging the gap between the boundary layer and the upper atmosphere. Many observed disturbances in the middle and upper layers originate from energetic processes in the lower atmosphere, yet the transmission mechanisms across these layers remain poorly constrained [20,21]. The integration of coherent and incoherent lidar systems offers a unique capability to trace this energy pathway: linking the initiation of disturbances (such as severe storms or frontal systems) in the lower troposphere with their manifestation in the upper atmosphere. Here, we report a hybrid lidar system that integrates incoherent and coherent approaches to enable real-time, multi-scale wind field detection across 50 m to 40 km altitude.

2. Description of the Method

Coherent Doppler wind lidar retrieves wind velocity through heterodyne detection. The atmospheric backscattered signal, which carries a Doppler frequency shift induced by the motion of scattering particles along the laser's line-of-sight (LOS), is superimposed with a frequency-stable local oscillator (LO) on a photodetector. The resulting photocurrent contains a beat frequency corresponding to the frequency offset between the received signal and the LO. The resulting analog beat signal is first digitized by an analog-to-digital converter (ADC) to obtain a time-domain signal. After digitization, the beat signal is transformed into the frequency domain, commonly using Fast Fourier Transform (FFT)-based spectral analysis, from which the Doppler frequency shift is estimated. The LOS wind velocity is then derived from the measured Doppler shift using the lidar Doppler equation [22,23].

Incoherent Doppler wind lidar retrieves wind velocity by detecting the frequency shift in molecular or aerosol backscattered light using high-precision optical frequency discriminators. Typical discriminators include FPIs [11,24], iodine vapor cells [6,25], Fizeau interferometer [26,27], Mach–Zehnder interferometer [28,29] and the Michelson interferometer [30]. In this system, a dual-channel FPI is used as a frequency discriminator for Rayleigh Doppler wind measurements.

The Rayleigh Doppler wind retrieval in this system is based on the double-edge technique. In this configuration, the two FPI edge channels are positioned on opposite sides of the emitted laser frequency, where their transmission curves exhibit steep and opposite

frequency responses. Due to the symmetric design, the transmitted laser frequency and the returned backscattered signal spectrum center will be set precisely at the crossover point of these curves when no Doppler shift is induced. When atmospheric motion occurs along the laser's LOS, the resulting Doppler-induced spectral displacement causes opposite changes in the transmitted signal intensities of the two edge channels. The Doppler frequency shift can therefore be inferred from the normalized intensity difference between the two channels.

When detecting an atmospheric motion along the laser LOS, the spectral displacement leads to opposite changes in the transmitted signal intensities of the two edge channels. The Doppler frequency shift can therefore be inferred from the normalized intensity difference between the two channels.

For a specified LOS direction, we define the response function $R(\nu)$ at each distance z in Equation (1):

$$R(\nu) = \frac{I_1(\nu_l + \Delta\nu) - I_2(\nu_l + \Delta\nu)}{I_1(\nu_l + \Delta\nu) + I_2(\nu_l + \Delta\nu)}, \quad (1)$$

where $I_1(\nu_l + \Delta\nu)$ and $I_2(\nu_l + \Delta\nu)$ denote the atmospheric backscattered signal intensities at distance z passing through the two edge channels, respectively. The response function $R(\nu)$ describes the relative spectral displacement of the atmospheric backscattered signal with respect to the transmission slopes of the two edge channels. As the two channels have opposite sensitivities to frequency shifts, small Doppler-induced spectral displacements can be converted into measurable variations in $R(\nu)$, which in turn yields the radial wind velocity V_{LOS}.

The velocity sensitivity Θ_ν represents the rate of change in the response function $R(\nu)$ per unit change from the spectral displacement from the Doppler shift shown in Equation (2):

$$\Theta_\nu = \frac{2}{\lambda R(\nu)} \frac{dR(\nu)}{d\nu}, \quad (2)$$

The radial wind velocity V_{LOS} can then be derived from Equation (2):

$$V_{LOS} = \frac{R(\nu)}{\Theta_\nu} = \frac{\lambda}{2} \frac{I_1(\nu_l + \Delta\nu) - I_2(\nu_l + \Delta\nu)}{I_1(\nu_l + \Delta\nu) + I_2(\nu_l + \Delta\nu)} \frac{d\nu}{dR(\nu)}, \quad (3)$$

3. Instrument Description

The lidar system proposed in this paper is designed to provide wind measurements from 50 m to 40 km in altitude. It consists of an incoherent Rayleigh Doppler lidar and a coherent Mie Doppler lidar, both with two-dimensional scanning capability. The coherent lidar is used to retrieve wind fields within the boundary layer (from 50 m above ground to the top of the boundary layer), where aerosol backscatter is relatively strong. The incoherent lidar covers wind field detection from the boundary layer up to 40 km, utilizing molecular backscatter. This section describes the system configuration, main instrumental parameters, and the wind retrieval methods.

3.1. System Overview

The wind lidar system developed in this study is named DWL40k, reflecting its design objective of wind profiling up to approximately 40 km altitude. A schematic diagram of the optical layout of the incoherent Doppler lidar is shown in Figure 1.

To avoid the influence of laser frequency jitter, the incoherent wind lidar in the DWL40k system employs a semiconductor-pumped, pulse-directly amplified frequency-tripled Nd:YAG laser (Quantel Merion MW, LUMIBIRD SA (35 Boulevard Solférino, 35000 Rennes, France)) [21]. It utilizes a narrow linewidth and wavelength-stable single-longitudinal-mode seed laser (NKT Y10 fiber laser, linewidth < 20 kHz, NKT Photonics (Bregnerødvej

144, 3460 Birkerød, Denmark)). The seed has an output power of 20 mW and a wavelength stability better than 100 MHz (over 10 min). The continuous light emitted by the seed laser is chopped by an acousto-optic modulator (AOM) and amplified to generate pulsed signals (13 μJ), which are injected into the solid-state laser. This was followed by two stages of semiconductor optical amplification, which further amplified the energy of each pulse. Finally, the system outputs laser pulses with an energy of 270 mJ and a repetition rate of 100 Hz.

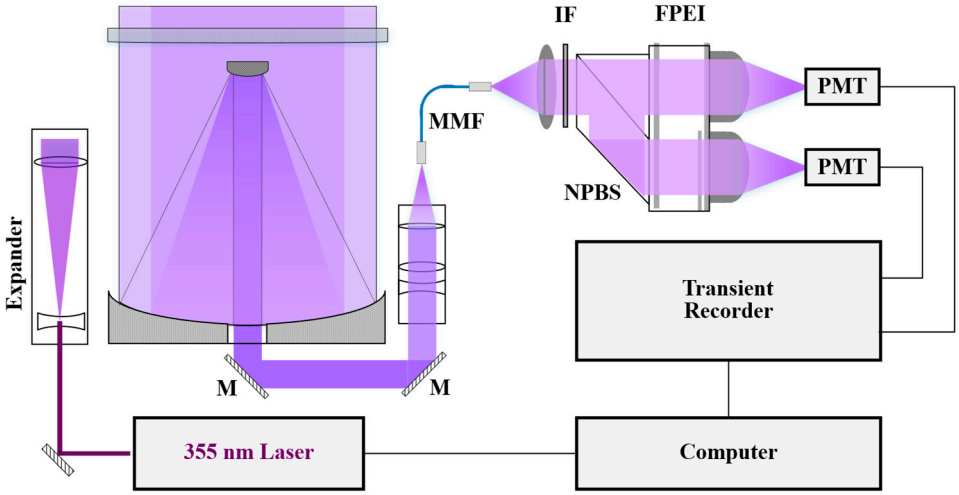

Figure 1. Schematic of the incoherent lidar optical setup. M, mirror; MMF, multi-mode fiber; IF, interference filter; NPBS, non-polarizing beam splitter; FPEI, Fabry–Perot etalon interferometer; PMT, photomultiplier.

The spectral distribution of the emitted laser pulses can be approximated by a Gaussian profile with a full width at half maximum (FWHM) of 500 MHz. This laser linewidth is significantly narrower than the spectral width of the atmospheric Rayleigh backscattered signal and the FWHM of the FPI edge channels, making it suitable for the Doppler frequency discrimination.

To achieve measurements at altitudes of up to 40 km, suppression of background contamination is essential. A narrow receiver field-of-view (FOV) is therefore adopted to reduce background noise. Accordingly, the divergence angle of the transmitted laser must also be reduced to maintain effective overlap between the transmitted beam and the receiver FOV. A beam expander is used to increase the laser beam diameter from 10 mm to 160 mm, thereby reducing the divergence angle of the transmitted laser beam.

During field observations, the incoherent lidar and the coherent lidar operate simultaneously. All components of the incoherent lidar, including the laser transmitter, the beam expander, the 1 m aperture telescope, and the optical receiver, are mounted on a two-dimensional scanning platform. For wind measurements, the transmitted beam and the telescope optical axis are pointed at a zenith angle of 30°. The azimuth angle is determined using a BeiDou differential antenna. Measurements are sequentially performed in the east, west, south, and north directions, and the corresponding radial wind velocities are combined to retrieve the horizontal wind components through vector synthesis.

The receiver of the incoherent Rayleigh Doppler lidar consists mainly of a non-polarizing beam splitter (NPBS), an interference filter (IF) module, photomultiplier tube (PMT) detectors, a double-edge FPI module, and associated collimation and focusing optics. To be noticed, the beam-splitting ratio of the NPBS is independent of the polarization state. During measurement, the atmospheric backscattered signal passes through the telescope and enters a multimode fiber with a core diameter of 200 μm. The fiber beam is collimated and expanded into a 20 mm parallel beam through a collimation system, which then passes

through the NPBS and enters the two channels of the FPI. The light from the dual-edge channels is focused by a lens into the PMT, where they are converted into electrical signals. The resulting electrical signals are recorded by a transient recorder to obtain the photon counts from the two edge channels.

In the overlap region, the incoherent lidar signal comprises both aerosol and molecular scattering components. To address this, we optimized the characteristics of the FPI so that the sensitivity of the aerosol signal matches that of the molecular scattering signal, as depicted in Figure 2. To improve the signal-to-noise ratio (SNR) of the received signals, the PMT model R9890 is employed, with a quantum efficiency of approximately 30% at 355 nm. The transient recorder utilizes a 16-bit analog-to-digital converter with a sampling frequency of 40 MHz. To enhance the mobility of the system, the incoherent wind lidar is installed on a truck-mounted platform. Key parameters of the Rayleigh Doppler lidar system components are provided in Table 1.

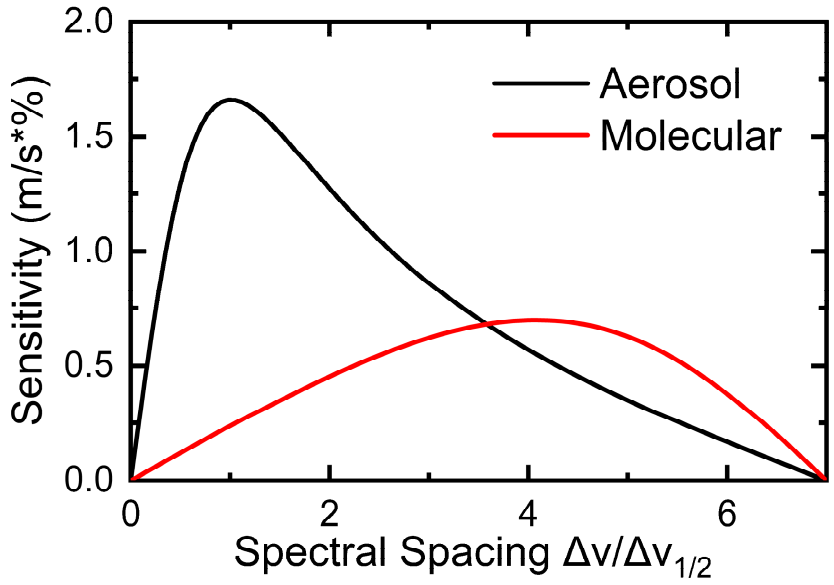

Figure 2. The Doppler sensitivity, i.e., percentage change in the normalized signal for a velocity of 1 m/s, plotted as a function of spectral spacing (in units of FWHM of the FPI).

Table 1. Key parameters of the mobile Rayleigh Doppler Lidar.

	Parameters	Value
Transmitter	Spatial resolution	100 m (<20 km), 200 m (<40 km)
	Wavelength	355 nm
	Pulse energy	270 mJ
	Repetition rate	100 Hz
Telescope	Aperture	1 m
	Field of view	0.09 mrad
	Zenith angle	30°
Receiver	FSR	9.2 GHz
	FWHM	1.31 GHz
	Edge channel separation	4.6 GHz
	Peak transmission	60%

The coherent wind lidar, which is used to measure wind fields within the boundary layer, is mounted on a liftable platform at the front of the truck. The coherent wind lidar

employs a coaxial telescope system with an aperture of 150 mm, a laser wavelength of 1550 nm, a single-pulse energy of 100 μJ, and a repetition rate of 10 kHz.

3.2. Retrieval of Horizontal Wind

The coherent and incoherent radars were linked via Ethernet and controlled by a common software interface to ensure temporal synchronization. During the experiment, both instruments were aligned to true north using fiber optic gyroscopes. Consistency in pointing direction was maintained by setting a zenith angle of 30° for both radars while acquiring wind fields through a four-beam scanning pattern. (See Figure 3).

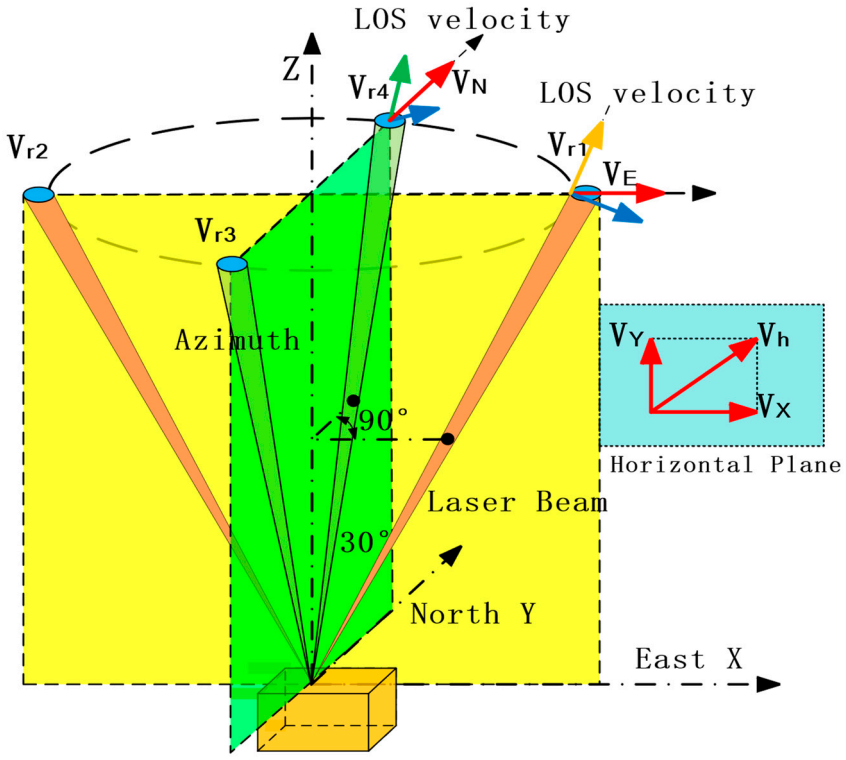

Figure 3. Schematic view of the lidar scanning geometry. Four detection directions are drawn for the eastward, westward, northward, and southward, each with a zenith angle of 30°.

To retrieve horizontal wind speed and direction, one assumption is adopted: the wind field remains approximately uniform during one complete scanning cycle (10 min). Under this assumption, the incoherent lidar first measures the LOS wind velocities in the west and east directions, followed by the north and south directions. The horizontal wind velocity components along the *X*-axis (East) and *Y*-axis (north) can be derived using the following equations:

$$V_X = \frac{V_E - V_W}{2\sin\varphi},\ V_Y = \frac{V_N - V_S}{2\sin\varphi}, \tag{4}$$

In Equation (4), V_X and V_Y represent the horizontal wind velocity components along the *X*-axis (east–west direction, with positive *X* as eastward) and *Y*-axis (north–south direction, with positive *Y* as northward). V_E, V_W, V_N and V_S denote the radial wind velocities measured when the telescope is pointed toward the east, west, north, and south directions, respectively. φ represents the zenith angle of the telescope, which equals 30°.

Based on the geometric relationship between V_X, V_Y and the horizontal wind velocity shown in Figure 3, the combined horizontal wind velocity V_h can be calculated using Equation (5).

$$V_h = \sqrt{V_X^2 + V_Y^2}, \tag{5}$$

The horizontal wind direction can be derived from Equation (6).

$$\theta_h = \arctan(V_X / V_Y) + \pi\{1 - \text{sign}[(V_Y + |V_Y|) \times V_X]\} \quad V_Y \neq 0, \tag{6}$$

Here, the unit of horizontal wind direction θ_h is in radians.

4. Results

The DWL-40k system (shown in Figure 4) was employed to measure wind fields in two locations: Hefei, Anhui province, and Ürümqi, Xinjiang province.



Figure 4. The DWL-40k system in the experiment.

To examine the consistency between the coherent and incoherent lidar measurements in their overlapping range, wind velocity measurements within the 1.9–2.1 km altitude interval were compared. Under post-rain conditions, when aerosol loading was relatively low, the two systems showed good agreement within this altitude range. This comparison provides cross-validation for the two lidar retrievals and supports the feasibility of combining their wind profiles. However, at lower altitudes, noticeable discrepancies were observed, mainly due to enhanced aerosol backscatter and geometric overlap effects of the Rayleigh Doppler wind retrievals. Therefore, a 2 km altitude was selected as the transition point for connecting the coherent and incoherent lidar wind profiles for the DWL-40k system.

To evaluate the wind measurements obtained by the DWL40k system, radiosonde observations were used for comparison. Figure 5 shows the vertical profiles of horizontal wind speed and direction measured by the DWL40k system and radiosondes at 02:00 LT on 17 February and 14 April. The lidar-derived wind profiles are generally consistent with the radiosonde observations, indicating that the DWL40k system can capture the main vertical structures of horizontal wind speed and direction during the field campaigns.

Figure 6 presents the time–altitude cross-section of the semi-continuous horizontal wind observations obtained by the DWL40k system in April 2024. The results show the temporal evolution and vertical distribution of horizontal wind velocity and direction from 50 m to 40 km in height. A quasi-zero wind layer (QZWL), characterized by a relatively weak horizontal wind speed, can be observed at approximately 20–24 km altitude.

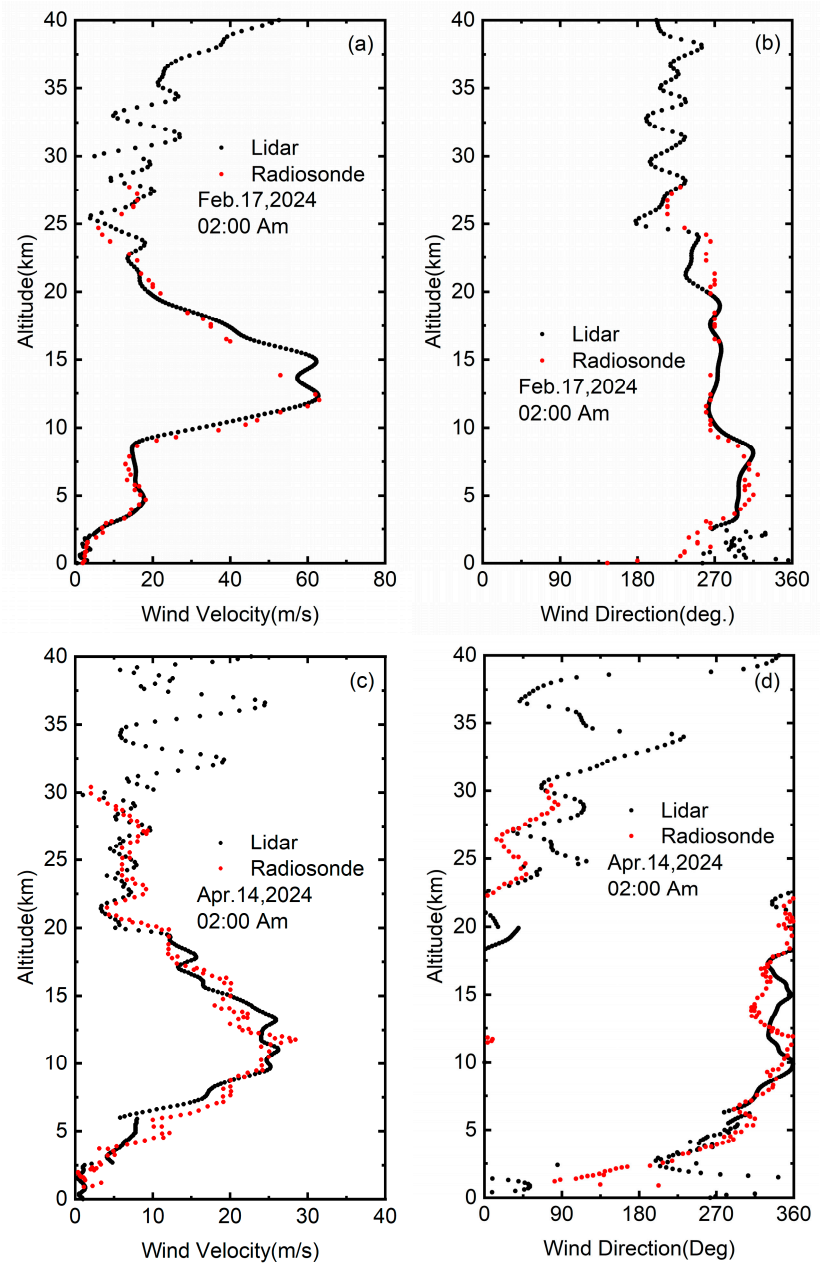

Figure 5. (**a**) Profiles of horizontal wind velocity measured by the DWL-40k system compared with data from the radiosonde at LT 02:00, 17 February; (**b**) Profiles of horizontal wind direction measured by the DWL-40k system compared with data from the radiosonde at LT 02:00, 17 February; (**c**) Profiles of horizontal wind velocity measured by the DWL-40k system compared with data from the radiosonde at LT 02:00, 14 April; (**d**) Profiles of horizontal wind velocity measured by the DWL-40k system compared with data from the radiosonde at LT 02:00, 14 April. The red dots represent data from the radiosonde, and the black dots represent data from the lidar system.

As can be seen from Figure 6, there is a significant anomaly in wind speed at the 5 km altitude on 7 and 9 April. A subsequent review of the raw data revealed the presence of thin clouds at the corresponding altitude, along with strong aerosol signals, which affected the accuracy of the wind speed measurements. On 12 April, cloud-induced detector saturation was observed, and the contaminated data within the affected altitude range were therefore excluded from further analysis. These results indicate that aerosol and cloud contamination can influence incoherent Rayleigh Doppler wind retrievals, particularly in the lower troposphere. At altitudes above 5 km, the influence of aerosol contamination was

substantially reduced, where the DWL40k wind profiles showed good consistency with radiosonde observations.

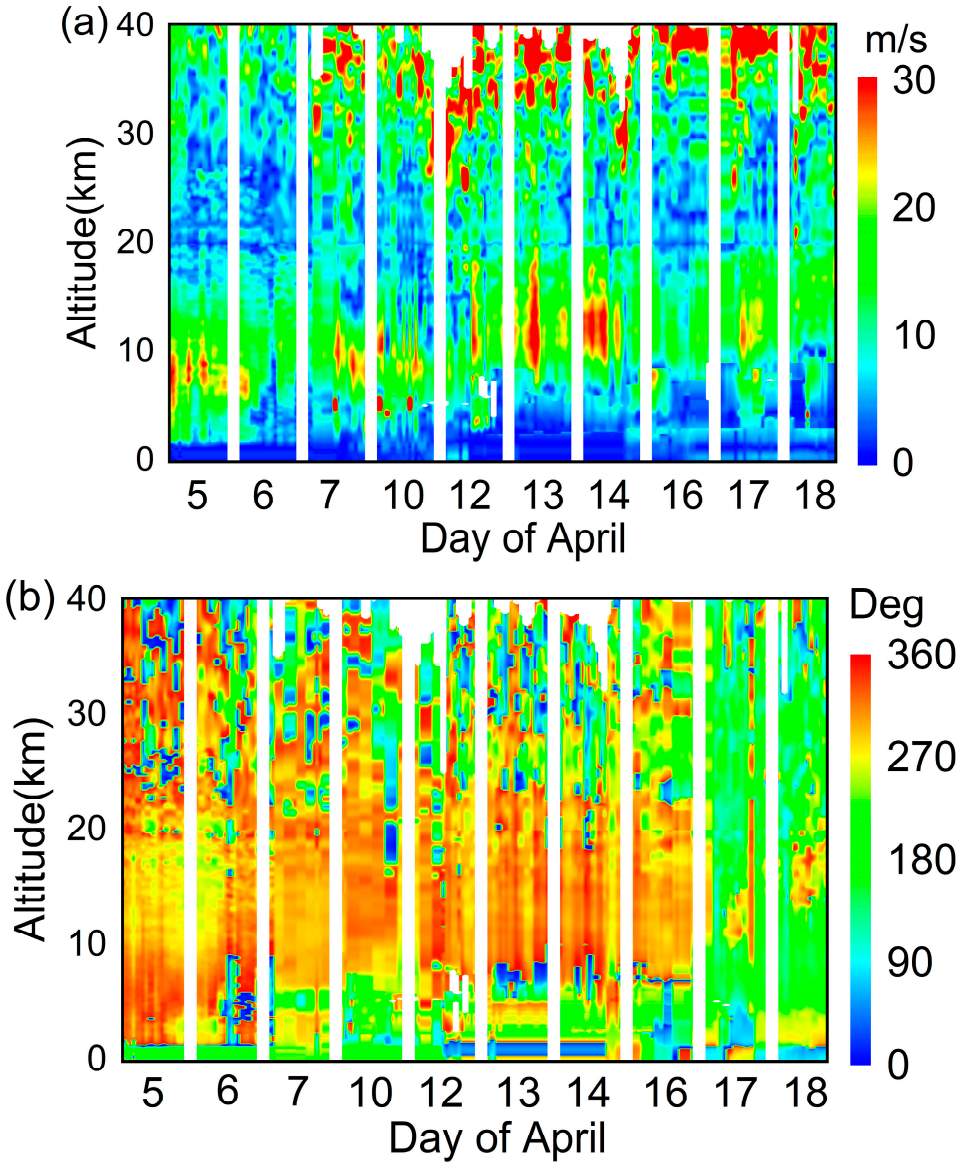

Figure 6. (**a**) Time-altitude cross-section of semi-continuous horizontal wind speed observed by DWL-40k system in April 2024; (**b**) Time-altitude cross-section of semi-continuous horizontal wind direction observed by DWL-40k system in April 2024.

To quantitatively evaluate the DWL40k system with radiosonde observations, we calculated the bias, standard deviation (STD), relative STD, and correlation coefficient for all measurements according to the definitions provided by Witschas et al. [31]. Figure 7 shows the statistical analysis of the wind speed difference between the lidar data and radiosonde data. Figure 7a shows the wind speed difference between the radiosonde data and data collected by the DWL40k around 02:00 on 17 February, for which the wind speed bias is 1.88 m/s and the standard deviation is 3.78 m/s. Figure 7b presents the wind speed difference between radiosonde data and DWL40k data around 02:00 on 14 April, with a wind speed bias of 0.62 m/s and a standard deviation of 0.64 m/s. The relatively small wind speed biases and standard deviations indicate good quantitative agreement between the DWL40k retrievals and the radiosonde observations in the representative field cases,

providing validation evidence for the credibility and reliability of the DWL40k system in vertically extended wind profiling.

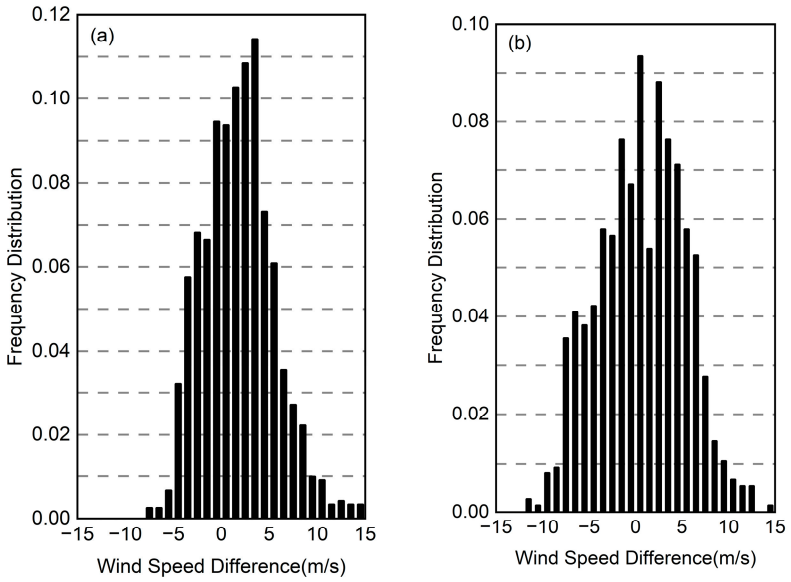

Figure 7. (**a**) Histogram of the wind speed difference between the DWL-40k system and the radiosonde measured on 17 February; (**b**) Histogram of the wind speed difference between the DWL-40k system and the radiosonde measured on 14 April.

5. Discussion

The wind field observations demonstrate the practical value of combining a coherent Doppler lidar and an incoherent Rayleigh Doppler lidar in a single mobile wind-profiling system. This complementary configuration, therefore, provides a practical approach for vertically extended wind observations from the boundary layer to the stratosphere.

The comparison with radiosonde observations further indicates that the DWL40k system can capture the main vertical structures of horizontal wind speed and direction. The relatively small bias and standard deviation obtained in representative cases suggest good consistency between the lidar retrievals and independent observations. Nevertheless, the observed differences should not be attributed solely to lidar retrieval errors. Radiosonde measurements are not strictly collocated with the lidar beam and may drift horizontally during ascent, while lidar retrievals represent range-resolved measurements along fixed scanning directions. Temporal averaging, spatial separation, and atmospheric variability can therefore contribute to the differences between the two datasets.

6. Conclusions

By employing both coherent and incoherent Doppler lidar simultaneously, the DWL40k system obtained vertically extended wind profiles spanning from 50 m to 40 km. The incoherent lidar is equipped with a 1 m aperture telescope, and both lidar units are installed on a truck-mounted platform to enhance system mobility. The spatial resolution of the incoherent lidar is 100 m below the 20 km altitude and 200 m above the 20 km, with a temporal resolution of 10 min.

As shown in Figure 4, the wind field data acquired by this system exhibits strong agreement with the results from the radiosonde measurements across the observed altitude range. Furthermore, the long-term observational data presented in Figure 5 demonstrates the high stability and reliability of the system over 10 days.

Author Contributions: Conceptualization, H.L. and Y.H.; methodology, H.L. and J.L. (Jie Liu); software, H.L.; validation, H.L., J.L. (Jie Liu) and S.W.; formal analysis, H.L.; investigation, Y.H. and D.S.; resources, J.L. (Jie Liu), S.Z. and C.C.; data curation, H.L. and J.L. (Jiawei Li); writing—original draft preparation, H.L.; writing—review and editing, H.L. and J.L. (Jiawei Li); visualization, H.L.; supervision, Y.H.; project administration, D.S.; funding acquisition, D.S. All authors have read and agreed to the published version of the manuscript.

Funding: This research was funded by the National Natural Science Foundation of China under (Grant Nos. 42374182 and 42104146) and the Innovation Program for Quantum Science and Technology (Grant No. 2021ZD0300302).

Data Availability Statement: Due to privacy concerns, the data are not publicly available, and access can be requested from the corresponding author.

Acknowledgments: During the preparation of this manuscript/study, the author used [Deepseek, V3.2] and [Chat GPT, V5.1] to improve the readability and language of the manuscript. The authors have reviewed and edited the output and take full responsibility for the content of this publication.

Conflicts of Interest: The authors declare no conflicts of interest.

References

1. Hays, P.B.; Dehring, M.T.; Fisk, L.A.; Tchoryk, P.; Wang, J. *Space-Based Doppler Winds LIDAR: A Vital National Need*; National Research Council (NRC): Ottawa, ON, Canada, 2005.
2. Schmidt, D.; Stevens, J.; Roney, J. Near-Space Station-Keeping Performance of a Large High-Altitude Notional Airship. In Proceedings of the AIAA Atmospheric Flight Mechanics Conference and Exhibit, Keystone, CO, USA, 21–24 August 2006.
3. Ishii, S.; Kishibuchi, K.; Takenaka, H.; Jin, Y.; Nishizawa, T.; Sugimoto, N.; Iwai, H.; Aoki, M.; Kawamura, S.; Okamoto, H. 355-nm direct-detection Doppler wind lidar for vertical atmospheric motion measurement. *Appl. Opt.* **2022**, *61*, 7925–7936. [CrossRef]
4. Garnier, A.; Chanin, M.-L. Description of a Doppler rayleigh LIDAR for measuring winds in the middle atmosphere. *Appl. Phys. B* **1992**, *55*, 35–40. [CrossRef]
5. Chanin, M.-L.; Garnier, A.; Hauchecorne, A.; Porteneuve, J. A Doppler lidar for measuring winds in the middle atmosphere. *Geophys. Res. Lett.* **1989**, *16*, 1273–1276. [CrossRef]
6. Friedman, J.S.; Tepley, C.A.; Castleberg, P.A.; Roe, H.G. Middle-atmospheric Doppler lidar using an iodine-vapor edge filter. *Opt. Lett.* **1997**, *22*, 1648–1650. [CrossRef]
7. Tepley, C.A. Neutral winds of the middle atmosphere observed at Arecibo using a Doppler Rayleigh lidar. *J. Geophys. Res.* **1994**, *99*, 25781–25790.
8. Tepley, C.A.; Sargoytchev, S.I.; Rojas, R. The Doppler Rayleigh lidar system at Arecibo. *IEEE Trans. Geosci. Remote Sens.* **1993**, *31*, 36–47. [CrossRef]
9. Tepley, C.A.; Sargoytchev, S.I.; Hines, C.O. Initial Doppler Rayleigh lidar results from Arecibo. *Geophys. Res. Lett.* **1991**, *18*, 167–170. [CrossRef]
10. Flesia, C.; Korb, C.L. Theory of the double-edge molecular technique for Doppler lidar wind measurement. *Appl. Opt.* **1999**, *38*, 432–440. [CrossRef]
11. Korb, C.L.; Gentry, B.M.; Li, S.X.; Flesia, C. Theory of the double-edge technique for Doppler lidar wind measurement. *Appl. Opt.* **1998**, *37*, 3097–3104. [CrossRef]
12. Han, Y.; Sun, D.; Han, F.; Liu, H.; Zhao, R.; Zhen, J.; Zhang, N.; Chen, C.; Li, Z. Demonstration of daytime wind measurement by using mobile Rayleigh Doppler Lidar incorporating cascaded Fabry-Perot etalons. *Opt. Express* **2019**, *27*, 34230–34246. [CrossRef]
13. Zhao, R.; Dou, X.; Xue, X.; Sun, D.; Han, Y.; Chen, C.; Zheng, J.; Li, Z.; Zhou, A.; Han, Y.; et al. Stratosphere and lower mesosphere wind observation and gravity wave activities of the wind field in China using a mobile Rayleigh Doppler lidar. *J. Geophys. Res. Space Phys.* **2017**, *122*, 8847–8857. [CrossRef]
14. Zhao, R.; Dou, X.; Sun, D.; Xue, X.; Zheng, J.; Han, Y.; Chen, T.; Wang, G.; Zhou, Y. Gravity waves observation of wind field in stratosphere based on a Rayleigh Doppler lidar. *Opt. Express* **2016**, *24*, A581–A591. [CrossRef]
15. Dou, X.; Han, Y.; Sun, D.; Xia, H.; Shu, Z.; Zhao, R.; Shangguan, M.; Guo, J. Mobile Rayleigh Doppler lidar for wind and temperature measurements in the stratosphere and lower mesosphere. *Opt. Express* **2014**, *22*, A1203–A1221. [CrossRef]
16. Baars, H.; Herzog, A.; Heese, B.; Ohneiser, K.; Hanbuch, K.; Hofer, J.; Yin, Z.; Engelmann, R.; Wandinger, U. Validation of Aeolus wind products above the Atlantic Ocean. *Atmos. Meas. Tech.* **2020**, *13*, 6007–6024. [CrossRef]
17. Marksteiner, U.; Lemmerz, C.; Lux, O.; Rahm, S.; Schäfler, A.; Witschas, B.; Reitebuch, O. Calibrations and wind observations of an airborne direct-detection wind LiDAR supporting ESA's Aeolus mission. *Remote Sens.* **2018**, *10*, 2056. [CrossRef]

18. Lux, O.; Lemmerz, C.; Weiler, F.; Marksteiner, U.; Witschas, B.; Rahm, S.; Schäfler, A.; Reitebuch, O. Airborne wind lidar observations over the North Atlantic in 2016 for the pre-launch validation of the satellite mission Aeolus. *Atmos. Meas. Tech.* **2018**, *11*, 3297–3322. [CrossRef]
19. Reitebuch, O. The Spaceborne Wind Lidar Mission ADM-Aeolus. In *Atmospheric Physics: Background–Methods–Trends*; Schumann, U., Ed.; Springer: Berlin, Germany, 2012; pp. 815–827.
20. Li, Q.; Xu, J.; Liu, H.; Liu, X.; Yuan, W. How do gravity waves triggered by a typhoon propagate from the troposphere to the upper atmosphere? *Atmos. Chem. Phys.* **2022**, *22*, 12077–12091. [CrossRef]
21. Plougonven, R.; Zhang, F. Internal gravity waves from atmospheric jets and fronts. *Rev. Geophys.* **2014**, *52*, 33–76. [CrossRef]
22. Kameyama, S.; Ando, T.; Asaka, K.; Hirano, Y.; Wadaka, S. Compact all-fiber pulsed coherent Doppler lidar system for wind sensing. *Appl. Opt.* **2007**, *46*, 1953–1962. [CrossRef]
23. Bilbro, J. Atmospheric Laser Doppler Velocimetry: An Overview. *Opt. Eng.* **1980**, *19*, 194533. [CrossRef]
24. Korb, C.L.; Gentry, B.M. New Doppler lidar methods for atmospheric wind measurements: The edge technique. In Proceedings of the Conference on Lasers and Electro-Optics, Baltimore, MD, USA, 21 May 1990.
25. Wang, Z.; Liu, Z.; Liu, L.; Wu, S.; Liu, B.; Li, Z.; Chu, X. Iodine-filter-based mobile Doppler lidar to make continuous and full-azimuth-scanned wind measurements: Data acquisition and analysis system, data retrieval methods, and error analysis. *Appl. Opt.* **2010**, *49*, 6960–6978. [CrossRef]
26. Witschas, B.; Vaughan, M.; Lux, O.; Lemmerz, C.; Nikolaus, I.; Reitebuch, O. Verification of different Fizeau fringe analysis algorithms based on airborne wind lidar data in support of ESA's Aeolus mission. *Appl. Opt.* **2023**, *62*, 7917–7930. [CrossRef]
27. Mckay, J.A. Assessment of a multibeam Fizeau wedge interferometer for Doppler wind lidar. *Appl. Opt.* **2002**, *41*, 1760–1767. [CrossRef]
28. Bruneau, D. Fringe-imaging Mach-Zehnder interferometer as a spectral analyzer for molecular Doppler wind lidar. *Appl. Opt.* **2002**, *41*, 503–510. [CrossRef]
29. Bruneau, D. Mach–Zehnder interferometer as a spectral analyzer for molecular Doppler wind lidar. *Appl. Opt.* **2001**, *40*, 391–399. [CrossRef]
30. Cézard, N.; Dolfi-Bouteyre, A.; Huignard, J.-P.; Flamant, P.H. Performance evaluation of a dual fringe-imaging Michelson interferometer for air parameter measurements with a 355 nm Rayleigh-Mie lidar. *Appl. Opt.* **2009**, *48*, 2321–2332. [CrossRef]
31. Witschas, B.; Lemmerz, C.; Geiß, A.; Lux, O.; Marksteiner, U.; Rahm, S.; Reitebuch, O.; Weiler, F. First validation of Aeolus wind observations by airborne Doppler wind lidar measurements. *Atmos. Meas. Tech.* **2020**, *13*, 2381–2396. [CrossRef]

Disclaimer/Publisher's Note: The statements, opinions and data contained in all publications are solely those of the individual author(s) and contributor(s) and not of MDPI and/or the editor(s). MDPI and/or the editor(s) disclaim responsibility for any injury to people or property resulting from any ideas, methods, instructions or products referred to in the content.